The Astrophysical Journal Letters, 776:L31 (6pp), 2013 October 20 doi:10.1088/2041-8205/776/2/L31

ENERGY FEEDBACK FROM X-RAY BINARIES IN THE EARLY UNIVERSE

T. Fragos[1,2], B. D. Lehmer[3,4], S. Naoz[2,7], A. Zezas[1,5,6], and A. Basu-Zych[4]

[1] Harvard-Smithsonian Center for Astrophysics, 60 Garden Street, Cambridge, MA 02138, USA; tfragos@cfa.harvard.edu

[2] Institute for Theory and Computation, Harvard-Smithsonian Center for Astrophysics, 60 Garden Street, Cambridge, MA 02138, USA

[3] The Johns Hopkins University, Homewood Campus, Baltimore, MD 21218, USA

[4] NASA Goddard Space Flight Centre, Code 662, Greenbelt, MD 20771, USA

[5] Department of Physics, University of Crete, P.O. Box 2208, 71003 Heraklion, Crete, Greece

[6] IESL, Foundation for Research and Technology, 71110 Heraklion, Crete, Greece

Received 2013 June 6; accepted 2013 September 18; published 2013 October 4

ABSTRACT

X-ray photons, because of their long mean-free paths, can easily escape the galactic environments where they are produced, and interact at long distances with the intergalactic medium, potentially having a significant contribution to the heating and reionization of the early universe. The two most important sources of X-ray photons in the universe are active galactic nuclei (AGNs) and X-ray binaries (XRBs). In this Letter we use results from detailed, large scale population synthesis simulations to study the energy feedback of XRBs, from the first galaxies ($z \sim 20$) until today. We estimate that X-ray emission from XRBs dominates over AGN at $z \gtrsim 6$–8. The shape of the spectral energy distribution of the emission from XRBs shows little change with redshift, in contrast to its normalization which evolves by ∼4 orders of magnitude, primarily due to the evolution of the cosmic star-formation rate. However, the metallicity and the mean stellar age of a given XRB population affect significantly its X-ray output. Specifically, the X-ray luminosity from high-mass XRBs per unit of star-formation rate varies an order of magnitude going from solar metallicity to less than 10% solar, and the X-ray luminosity from low-mass XRBs per unit of stellar mass peaks at an age of ∼300 Myr and then decreases gradually at later times, showing little variation for mean stellar ages $\gtrsim$3 Gyr. Finally, we provide analytical and tabulated prescriptions for the energy output of XRBs, that can be directly incorporated in cosmological simulations.

Key words: dark ages, reionization, first stars – galaxies: high-redshift – galaxies: stellar content – stars: evolution – X-rays: binaries – X-rays: diffuse background

Online-only material: machine-readable table

1. INTRODUCTION

An important cosmic milestone is the appearance of the first luminous objects, which ends the era of the cosmic dark ages and begins the era of heating and reionization of the intergalactic medium (IGM). The energy and momentum output from stars is believed to be a major feedback mechanism, along with the feedback from active galactic nuclei (AGNs), that regulate galaxy formation and the reionization epoch (e.g., Springel et al. 2005; Sales et al. 2010; Hopkins et al. 2011; Dib 2011; Faucher-Giguère et al. 2013). To date, the vast majority of cosmological simulation studies consider only the feedback from massive O stars and AGN via their ionizing ultraviolet (UV) radiation and deposition of mechanical energy and momentum in the vicinities of star-forming regions and accreting supermassive black holes (BHs; e.g., McQuinn et al. 2007a; Stinson et al. 2013; Sobacchi & Mesinger 2013).

UV photons are easily absorbed by neutral hydrogen, and they are efficient in ionizing it. Since the energy output of massive stars and AGN peaks at UV wavelengths the radiation from the first galaxies is expected to eventually ionize the neighboring IGM. The Swiss-cheese paradigm, in which the neutral background gas is spotted with spherical regions of hot and ionized gas by starburst galaxies and quasars (e.g., McQuinn et al. 2007b), is widely accepted (e.g., Loeb & Barkana 2001).

On the contrary, the more energetic X-ray photons, because of their long mean-free paths, can escape the galactic environments where they are produced, and interact at Mpc scales with the IGM. This could potentially result in a smoother spatial distribution of ionized regions (e.g., Ostriker & Gnedin 1996; Pritchard & Furlanetto 2007), and perhaps more importantly, in an overall warmer IGM (e.g., Mirabel et al. 2011; Haiman 2011). The two most important sources of X-ray photons in the universe are AGN and X-ray binaries (XRBs). Current constraints show that AGN provide at least an order-of-magnitude higher X-ray luminosity per unit volume over XRBs from $z \approx 0$–3 (e.g., Basu-Zych et al. 2013a). These constraints indicate that the X-ray luminosity per unit volume for XRBs begins to "catch up" to that of AGN going to the highest measurable redshifts (e.g., $z \approx 3$–4). Therefore, it is plausible that at even higher redshifts ($z \gtrsim 4$–5), the X-ray emission from XRBs becomes important or even dominant.

The possible feedback processes from XRBs at high redshifts ($z \gtrsim 6$) has been the topic of several papers in the last few years. Mirabel et al. (2011) considered primordial population-III (POP-III) binaries ($z \geqslant 6$), and proposed that besides the UV radiation from massive stars, feedback from accreting BHs in high-mass XRBs (HMXBs) was an additional, important source of heating and reionization of the IGM. Justham & Schawinski (2012) studied how XRBs inject energy in their local environments before luminous supernovae (SNe) contribute significantly to feedback. They argue that XRBs can also assist in keeping gas hot long after the last core-collapse SN has exploded. Power et al. (2013) explored the ionizing power of HMXBs at high redshifts using simple Monte Carlo modeling for their formation and the Galactic HMXB Cygnus X-1 as a spectral template for their emission in X-rays.

[7] Einstein Fellow.

In this Letter, we go for the first time beyond the order-of-magnitude calculations or simple rate models for the evolution of XRBs on cosmological timescales. We use results from a detailed large scale population synthesis simulation of the evolution of XRBs across cosmic time (Fragos et al. 2013), which has been calibrated to all available observations of XRB populations in the local and low redshift universe ($z \lesssim 4$), to study the energy output of XRBs at high redshift ($z \gtrsim 6$–8). We compare our model with the X-ray emission of AGN at the same redshifts and derive prescriptions for the feedback of XRBs that can be incorporated in future cosmological simulations.

2. X-RAY BINARY POPULATION SYNTHESIS MODELS

Using the `StarTrack` population synthesis code (Belczynski et al. 2002, 2008), Fragos et al. (2013) performed a large scale population synthesis study that models the XRB populations from the first galaxies of the universe until today. They used as input to their modeling the Millennium II Cosmological Simulation (Boylan-Kolchin et al. 2009) and the updated semi-analytic galaxy catalog by Guo et al. (2011) to self-consistently account for the star-formation history (SFH) and metallicity evolution of the universe. Their models, which were constrained by the observed X-ray properties of local galaxies (Tzanavaris & Georgantopoulos 2008; Lehmer et al. 2010; Boroson et al. 2011; Mineo et al. 2012a), gave predictions about the global scaling of emission from XRB populations with properties such as SFR and stellar mass, and the evolution of these relations with redshift. Although these models were only constrained to observations of the local universe, they have been shown to be in excellent agreement with X-ray observations of high redshift normal galaxies (Mineo et al. 2012b; Tremmel et al. 2013; Basu-Zych et al. 2013a, 2013b).

In this work, we adopt the six highest likelihood models by Fragos et al. (2013) which were also the six models which satisfy within one standard deviation all the observational constraints simultaneously (see discussion in Section 4.2 of Fragos et al. 2013). Instead of just choosing the maximum likelihood model, we assume that the differences among these six models represent in some sense the uncertainty in the model's predictions with regard to the redshift evolution of global scaling relations of emission from XRB populations.

We should not here that the population synthesis models we use assume an initial mass function (IMF) that does not evolve with redshift. However, there are theoretical arguments and indirect observational evidence suggest that the stellar IMF may evolve with time, becoming flatter at higher redshift (e.g., van Dokkum 2008). Fragos et al. (2013) showed that a flatter IMF results to more luminous XRB populations. Furthermore, our models are applicable to stellar population with metallicities down to $Z = 10^{-4}$, and do not take into account the first generation of metal-free POP-III star, which can potentially have significantly different evolution compared to enriched populations.

3. ENERGY OUTPUT OF THE X-RAY BINARY POPULATION

The emission of X-ray photons in the local universe is dominated by AGN, whose X-ray flux is approximately an order of magnitude stronger than that coming from XRB populations of normal galaxies. This picture is gradually changing as we move to higher redshifts, with the X-ray luminosity density coming from normal galaxies increasing faster than from AGN. The left panel of Figure 1 shows the redshift evolution of the X-ray luminosity density (X-ray luminosity per unit co-moving volume L_X/V) coming from XRBs, as predicted by the models of Fragos et al. (2013). On the same figure, several models and observational estimates for the X-ray luminosity density of AGN, as a function of redshift, are shown (Croton et al. 2006; Hopkins et al. 2007; Silverman et al. 2008; Aird et al. 2010). It is evident that at $z \gtrsim 6$–8, XRBs dominate the X-ray luminosity density, since the massive BHs at the centers of galaxies did not have enough time yet to grow and outshine the XRBs.

For comparison, we also show the contribution from XRBs that one would get if the locally measured value of the X-ray luminosity from HMXBs per unit of SFR (L_X/SFR; Mineo et al. 2012a) is convolved with the SFH of the universe. The adopted SFH comes from the Millennium II simulation (Boylan-Kolchin et al. 2009; Guo et al. 2011). We see that the contribution of XRBs is underestimated both at low and at high redshift. At low redshift, the contribution from low-mass XRBs (LMXB) is neglected as the measurement by Mineo et al. (2012a) was focused on the HMXB emission of starburst galaxies. We should remind here that in the local universe it is the LMXBs that are dominating the XRB luminosity density of the universe, with HMXBs starting to dominate only at $z \gtrsim 2.5$ (Fragos et al. 2013). At high redshift, a simple convolution of the locally measured L_X/SFR with the SFH neglects the effects of metallicity evolution on the stellar population. As we will show below, the X-ray luminosity from HMXBs per unit SFR varies by approximately an order of magnitude with metallicity.

3.1. Evolution of the Spectral Energy Distribution with Redshift

Our population synthesis models keep track of the mass-transfer rate as a function of time for every modeled XRB. From this mass-transfer rate, the bolometric luminosity is derived based on the prescriptions presented by Fragos et al. (2008, 2009), which also account for transient behavior of XRBs. However, there is no spectral information in these models. As described in detail in Section 3 of Fragos et al. (2013), we use two samples of *RXTE* observations of Galactic neutron star (NS) and BH XRBs at different spectral states (McClintock & Remillard 2006; Wu et al. 2010), for which the best-fit parameters of simple spectral models are calculated. Using these best-fit spectral models, and assuming that the interstellar absorption in high redshift galaxies is similar to that in the Milky Way today, we calculate for each energy band the mean and the variance of the bolometric correction for the high–soft and low–hard states, and BH and NS XRBs separately. Combining these bolometric corrections with our population synthesis models allows us to estimate the spectral energy distribution (SED) of a XRB population. In addition, we estimate the intrinsic XRB SED (without interstellar absorption) by removing the absorption component of the observed spectral models while making the assumption that the power-law component in the high and very high state does not extend to energies below ~1 KeV, and in the low–hard state below ~0.2 KeV (Sobolewska & Życki 2006). This allows the reader to apply a posteriori a more complicated model for interstellar absorption that can evolve with redshift.

The right panel of Figure 1 shows the SED per unit co-moving volume of the global XRB population at four different redshift values. We should note here that this SED corresponds to the radiation that escapes the galaxy where the photons are produced, as the interstellar absorption is already taken into account. These photons that escape the galaxy can then interact with the IGM. We find that the shape of the SED remains approximately

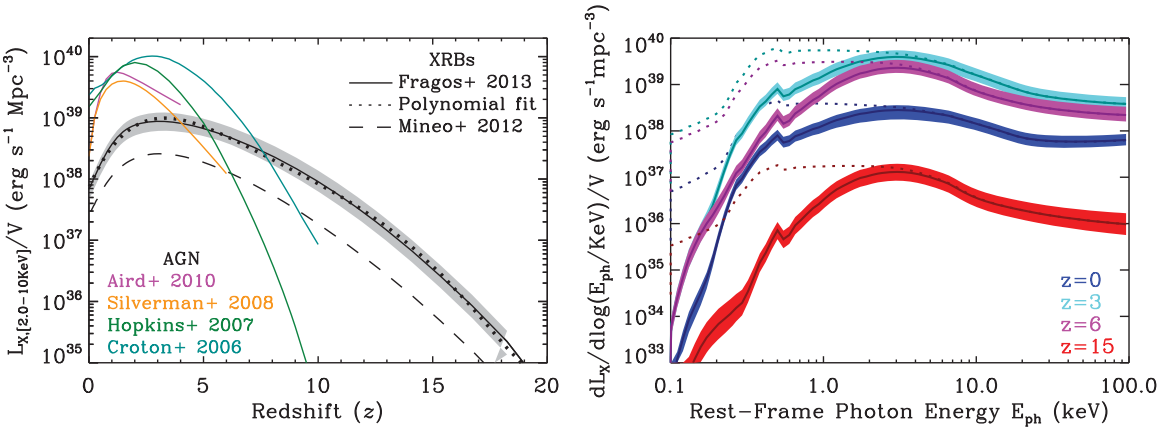

Figure 1. Left panel: X-ray luminosity per unit co-moving volume in the 2–10 KeV band as a function of redshift. The gray shaded area shows the differences between the predictions of the six highest likelihood models by Fragos et al. (2013) for the X-ray emission coming from XRBs. The black solid line corresponds to the mean value, and the dotted dark-gray line to the polynomial fit on the mean (Equation (2)). The dashed line is derived by convolving the locally measured value of L_X/SFR (Mineo et al. 2012a) with the SFH of the universe. For comparison the X-ray luminosity density of AGN in the same energy range is plotted, as reported by different AGN models and observations (Croton et al. 2006; Hopkins et al. 2007; Silverman et al. 2008; Aird et al. 2010). Right panel: the SED of the global XRB population at four different redshifts is shown. The solid lines correspond to the mean value of the different models and the shaded area denotes the model uncertainties, assuming in both cases that the interstellar absorption is similar to the Milky Way at all redshifts. With dotted lines we show an estimate of the intrinsic (unabsorbed) SED.

Table 1
Synthetic SED Data at Different Redshifts ($F(E_{\rm ph}) = dL_X/d\log(E_{\rm ph}/{\rm KeV})/V$ (erg s^{-1}Mpc^{-3}))

SED that includes interstellar absorption							
$E_{\rm ph}$	$F(E_{\rm ph})$ @ $z = 19.92$	$F(E_{\rm ph})$ @ $z = 18.24$	$F(E_{\rm ph})$ @ $z = 16.72$	$F(E_{\rm ph})$ @ $z = 15.34$	$F(E_{\rm ph})$ @ $z = 14.09$	$F(E_{\rm ph})$ @ $z = 12.94$	...
1.020E+00	4.590E+34	2.969E+35	1.139E+36	3.455E+36	9.036E+36	2.034E+37	...
1.115E+00	5.875E+34	3.799E+35	1.458E+36	4.419E+36	1.155E+37	2.598E+37	...
1.219E+00	7.256E+34	4.692E+35	1.800E+36	5.455E+36	1.425E+37	3.204E+37	...
1.333E+00	8.491E+34	5.490E+35	2.106E+36	6.380E+36	1.667E+37	3.745E+37	...
1.457E+00	9.874E+34	6.383E+35	2.448E+36	7.417E+36	1.937E+37	4.351E+37	...
1.593E+00	1.139E+35	7.364E+35	2.824E+36	8.555E+36	2.234E+37	5.016E+37	...
1.741E+00	1.283E+35	8.291E+35	3.179E+36	9.630E+36	2.514E+37	5.645E+37	...
1.903E+00	1.377E+35	8.898E+35	3.412E+36	1.033E+37	2.698E+37	6.056E+37	...
2.080E+00	1.495E+35	9.665E+35	3.706E+36	1.122E+37	2.930E+37	6.576E+37	...
⋮	⋮	⋮	⋮	⋮	⋮	⋮	⋱
Intrinsic (unabsorbed) SED							
$E_{\rm ph}$	$F(E_{\rm ph})$ @ $z = 19.92$	$F(E_{\rm ph})$ @ $z = 18.24$	$F(E_{\rm ph})$ @ $z = 16.72$	$F(E_{\rm ph})$ @ $z = 15.34$	$F(E_{\rm ph})$ @ $z = 14.09$	$F(E_{\rm ph})$ @ $z = 12.94$	...
1.020E+00	2.288E+35	1.478E+36	5.666E+36	1.716E+37	4.476E+37	1.004E+38	...
1.115E+00	2.323E+35	1.500E+36	5.753E+36	1.742E+37	4.545E+37	1.020E+38	...
1.219E+00	2.331E+35	1.505E+36	5.773E+36	1.748E+37	4.559E+37	1.023E+38	...
1.333E+00	2.339E+35	1.510E+36	5.791E+36	1.753E+37	4.573E+37	1.026E+38	...
1.457E+00	2.331E+35	1.505E+36	5.771E+36	1.747E+37	4.557E+37	1.022E+38	...
1.593E+00	2.339E+35	1.510E+36	5.790E+36	1.753E+37	4.572E+37	1.026E+38	...
1.741E+00	2.332E+35	1.506E+36	5.772E+36	1.747E+37	4.558E+37	1.023E+38	...
1.903E+00	2.319E+35	1.497E+36	5.740E+36	1.738E+37	4.533E+37	1.017E+38	...
2.080E+00	2.305E+35	1.488E+36	5.706E+36	1.727E+37	4.505E+37	1.011E+38	...
⋮	⋮	⋮	⋮	⋮	⋮	⋮	⋱

(This table is available in its entirety in a machine-readable form in the online journal. A portion is shown here for guidance regarding its form and content.)

constant with redshift, and it is only its normalization that evolves by ∼4 orders of magnitude (see left panel of Figure 1 and discussion above). The approximately constant SED shape is due to the fact that at all redshifts it is only the brightest BH XRBs in high states that dominate the integrated spectra. This is something to be expected from the shape of the X-ray luminosity functions of observed XRB populations in nearby galaxies. The shape of the X-ray luminosity functions of both LMXBs and HMXBs can be approximated by single power laws, which have exponents less than 2 ($(dN/dL_X) \propto L_X^{-n}$, with $n < 2$; Fabbiano 2006, and references therein). Hence, the integrated luminosity of the whole population is always dominated by the few brightest sources that are usually BH XRBs in the high–soft state. The SED data, both including interstellar absorption and intrinsic, at different redshift values can be found in Table 1.

Our model of the evolving X-ray luminosity density and mean X-ray SED can be used to estimate the contribution that XRBs in galaxies from $z = 0$–20 provide to the cosmic X-ray background. We integrated these models following:

$$S_{\rm tot} = \frac{\Delta\Omega}{4\pi}\frac{c}{H_0}\int_0^{20}\frac{\rho_X(z)K(z)dz}{(1+z)^2\varepsilon(z)}, \quad (1)$$

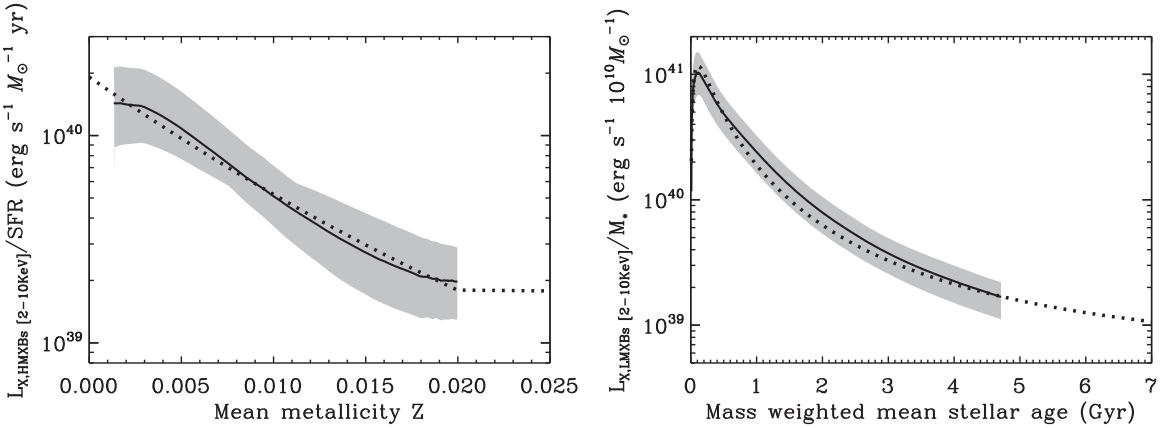

Figure 2. X-ray luminosity in the 2–10 KeV band of the HMXB population, per unit SFR, as a function of the mean metallicity Z of the newly formed stars (left panel) and X-ray luminosity in the 2–10 KeV band of the LMXB population, per unit stellar mass, as a function of the mass-weighted mean stellar age of stellar population. The gray shaded area shows the differences between the predictions of the six highest likelihood models by Fragos et al. (2013), the solid lines corresponds to the mean value of the different models, and the dotted lines show the polynomial fits on the mean, described in Equations (3) and (4).

where $\Delta\Omega = 3.0 \times 10^{-4}$ sr deg^{-2}, $\varepsilon(z) = \sqrt{\Omega_m(1+z)^3 + \Omega_\Lambda}$, ρ_X is the X-ray luminosity density from our model (see left panel of Figure 1), and $K(z)$ provides the redshift-dependent K-correction to the appropriate observed-frame energy range. The K-corrections are based on the SEDs shown in the right panel of Figure 1. Applying this integration to the observed-frame 0.5–2 keV bandpass, we find that XRB emission from all $z = 0$–20 galaxies is expected to contribute $S_{0.5-2\,\mathrm{keV}} \approx 2.2 \times 10^{-12}$ erg cm^{-2} s^{-1} deg^{-2} to the cosmic X-ray background intensity. By comparison, Lehmer et al. (2012) found that X-ray detected normal galaxies in the 4 Ms *Chandra* Deep Field-South contribute 2.4×10^{-13} erg cm^{-2} s^{-1} deg^{-2} to the resolved 0.5–2 keV background, and an additional 2.0×10^{-12} erg cm^{-2} s^{-1} deg^{-2} of the background remains unresolved. Our model is therefore within the allowed limits of the cosmic X-ray background (also in agreement with constraints derived by Dijkstra et al. 2012). Our analysis indicates that XRBs in normal galaxies can account for up to ∼98% of the remaining unresolved 0.5–2 keV emission. This estimate is only an upper limit as we did not take into account the absorption of X-ray photons from the IGM. In practice, we expect the contribution of XRBs to the observed cosmic X-ray background to be significantly lower.

3.2. Prescriptions for the Energy Feedback of LMXB and HMXB Populations

Our population synthesis modeling uses as input the SFH and metallicity evolution predicted by the Millennium II simulation. As a consequence, our results depend on the cosmological model and the galaxy formation and evolution prescriptions used by Boylan-Kolchin et al. (2009) and Guo et al. (2011), respectively. In order to alleviate this caveat, we extracted from our models the dependence of the X-ray luminosity of HMXBs per unit SFR ($L_{X,\mathrm{HMXBs}}/\mathrm{SFR}$) on the mean metallicity (Z) of the newly formed stars and the dependence of the X-ray luminosity coming from LMXBs per unit of stellar mass ($L_{X,\mathrm{LMXBs}}/M_*$) on the mass-weighted mean stellar age (T) of the population. Figure 2 shows that $L_{X,\mathrm{HMXBs}}/\mathrm{SFR}$ varies by an order of magnitude going from solar metallicity to less than 10% solar. This also indicates that at the era when HMXBs were dominating the X-ray radiation of the universe $L_{X,\mathrm{HMXBs}}/\mathrm{SFR}$ was approximately an order of magnitude higher than what is measured in the local universe (at $z \gtrsim 8$, $Z \lesssim 20\%\, Z_\odot$). The variation of $L_{X,\mathrm{LMXBs}}/M_*$ with the mean stellar age of the population is even stronger, peaking early on at stellar population ages of ∼300 Myr and then gradually decreasing to the values observed in the local universe. We should note here that the dependence of $L_{X,\mathrm{LMXBs}}/M_*$ with stellar age, for ages above ∼3 Gyr, becomes very weak, with an expected variation between ages of ∼3 Gyr and ∼13 Gyr of only a factor of a few (for related observational evidence see Boroson et al. 2011; Zhang et al. 2012).

Equations (2)–(4) are polynomial parameterizations to our model predictions for the evolution of the X-ray luminosity density of all XRBs as a function of redshift, the dependence of the X-ray luminosity coming from HMXBs per unit SFR on the mean metallicity (Z) of the newly formed stars, and the dependence of the X-ray luminosity of LMXBs per unit of stellar mass on the mass-weighted mean stellar age of the population (T) respectively. These polynomial parameterizations are shown in Figures 1 and 2 as dotted lines:

$$\log(L_X/V) = \alpha_0 + \alpha_1 z + \alpha_2 z^2 + \alpha_3 z^3 + \alpha_4 z^4 + \alpha_5 z^5 \times (\mathrm{erg\,s^{-1}\,pc^{-3}}), \quad \text{where } 0 \geqslant z \geqslant 20 \tag{2}$$

$$\log(L_X/\mathrm{SFR}) = \beta_0 + \beta_1 Z + \beta_2 Z^2 + \beta_3 Z^3 + \beta_4 Z^4 \times (\mathrm{erg\,s^{-1}}\, M_\odot^{-1}\,\mathrm{yr}), \quad \text{where } 0 \geqslant Z \geqslant 0.025 \tag{3}$$

$$\log(L_X/M_*) = \gamma_0 + \gamma_1 \log(T/\mathrm{Gyr}) + \gamma_2 \log(T/\mathrm{Gyr})^2 + \gamma_3 \log(T/\mathrm{Gyr})^3 + \gamma_4 \log(T/\mathrm{Gyr})^4 \times (\mathrm{erg\,s^{-1}}\, 10^{10}\, M_\odot^{-1}) \quad \text{where } 0 \geqslant T \geqslant 13.7\,\mathrm{Gyr}. \tag{4}$$

The parameters α_i ($i = 0, 5$), β_j ($j = 0, 4$), and γ_k ($k = 0, 4$) are derived for several widely used energy bands, both before and after taking into account interstellar absorption. The different parameter values are provided in Table 2.

4. DISCUSSION

Detailed binary population synthesis simulations are used for the first time in order to study the energy feedback of XRBs to the IGM, from $z \sim 20$ until today. Our synthetic XRB models capture accurately all the important physical processes that are

Table 2
List of Best-fit Parameter Values for Equations (2)–(4), Corresponding to Different Energy Bands

Energy Band	α_0	α_1	α_2	α_3	α_4	α_5	χ^2/N
Based on SED that includes interstellar absorption							
0.3–8.0 keV	37.84 ± 0.01	0.85 ± 0.02	-0.213 ± 0.008	0.0212 ± 0.0012	-0.00101 ± 0.00007	0.000018 ± 0.000002	0.09
0.5–2.0 keV	37.01 ± 0.01	0.86 ± 0.02	-0.221 ± 0.008	0.0221 ± 0.0012	-0.00106 ± 0.00007	0.000019 ± 0.000002	0.10
2.0–10.0 keV	37.86 ± 0.01	0.85 ± 0.02	-0.213 ± 0.008	0.0212 ± 0.0012	-0.00101 ± 0.00007	0.000018 ± 0.000002	0.09
10–100 keV	38.39 ± 0.02	0.73 ± 0.02	-0.188 ± 0.010	0.0188 ± 0.0014	-0.00091 ± 0.00009	0.000016 ± 0.000002	0.14
	β_0	β_1	β_2	β_3	β_4		
0.3–8.0 keV	40.28 ± 0.02	-62.19 ± 1.32	570.07 ± 13.71	-1835.81 ± 52.14	1970.48 ± 66.27		0.1751
0.5–2.0 keV	39.38 ± 0.02	-61.68 ± 1.31	565.42 ± 13.64	-1820.96 ± 51.88	1954.61 ± 65.94		0.1734
2.0–10.0 keV	40.28 ± 0.02	-62.12 ± 1.32	569.44 ± 13.71	-1833.80 ± 52.14	1968.33 ± 66.27		0.1751
10–100 keV	40.54 ± 0.02	-61.48 ± 1.35	563.60 ± 13.99	-1814.95 ± 53.20	1948.02 ± 67.61		0.1823
	γ_0	γ_1	γ_2	γ_3	γ_4		
0.3–8.0 keV	40.259 ± 0.014	-1.505 ± 0.016	-0.421 ± 0.025	0.425 ± 0.009	0.135 ± 0.009		1.3741
0.5–2.0 keV	39.455 ± 0.014	-1.514 ± 0.016	-0.455 ± 0.025	0.433 ± 0.009	0.145 ± 0.009		1.4254
2.0–10.0 keV	40.276 ± 0.014	-1.503 ± 0.016	-0.423 ± 0.025	0.425 ± 0.009	0.136 ± 0.009		1.3821
10–100 keV	40.717 ± 0.016	-1.417 ± 0.018	-0.369 ± 0.027	0.394 ± 0.010	0.111 ± 0.009		1.6787
Based on intrinsic (unabsorbed) SED							
	α_0	α_1	α_2	α_3	α_4	α_5	χ^2/N
0.3–8.0 keV	37.96 ± 0.01	0.86 ± 0.02	-0.213 ± 0.008	0.0211 ± 0.0012	-0.00100 ± 0.00007	0.000018 ± 0.000002	0.09
0.5–2.0 keV	37.36 ± 0.01	0.87 ± 0.02	-0.214 ± 0.008	0.0211 ± 0.0012	-0.00100 ± 0.00007	0.000018 ± 0.000001	0.09
2.0–10.0 keV	37.89 ± 0.01	0.86 ± 0.02	-0.214 ± 0.008	0.0213 ± 0.0012	-0.00101 ± 0.00007	0.000018 ± 0.000002	0.10
10–100 keV	38.38 ± 0.02	0.73 ± 0.02	-0.190 ± 0.010	0.0190 ± 0.0014	-0.00091 ± 0.00009	0.000016 ± 0.000002	0.14
	β_0	β_1	β_2	β_3	β_4		
0.3–8.0 keV	40.43 ± 0.02	-62.39 ± 1.32	571.82 ± 13.71	-1841.42 ± 52.14	1976.47 ± 66.28		0.1751
0.5–2.0 keV	39.87 ± 0.02	-62.48 ± 1.32	572.71 ± 13.71	-1844.27 ± 52.15	1979.52 ± 66.29		0.1752
2.0–10.0 keV	40.33 ± 0.02	-62.20 ± 1.32	570.19 ± 13.70	-1836.17 ± 52.09	1970.86 ± 66.21		0.1748
10–100 keV	40.54 ± 0.02	-61.34 ± 1.34	562.26 ± 13.88	-1810.59 ± 52.81	1943.31 ± 67.13		0.1797
	γ_0	γ_1	γ_2	γ_3	γ_4		
0.3–8.0 keV	40.370 ± 0.016	-1.581 ± 0.018	-0.495 ± 0.028	0.446 ± 0.010	0.157 ± 0.010		1.774
0.5–2.0 keV	39.795 ± 0.022	-1.746 ± 0.025	-0.669 ± 0.037	0.496 ± 0.014	0.207 ± 0.013		3.199
2.0–10.0 keV	40.308 ± 0.015	-1.525 ± 0.017	-0.445 ± 0.026	0.431 ± 0.009	0.142 ± 0.009		1.482
10–100 keV	40.716 ± 0.016	-1.418 ± 0.018	-0.370 ± 0.027	0.394 ± 0.010	0.112 ± 0.009		1.652

involved in the evolution of an XRB population, and have been calibrated to observed XRB population in the local universe. At the same time these synthetic models are in excellent agreement with X-ray observation of distant normal galaxies up to $z \sim 4$, thus providing a robust framework to study the evolution of XRB populations across cosmic time.

We find that the energetic X-ray photons emitted from XRBs dominate the X-ray radiation field over AGN at $z \gtrsim 6$–8, and hence XRB feedback can be a non-negligible contributor to the heating and reionization of the IGM in the early universe. The SED shape of the XRB emission does not change significantly with redshift, suggesting that the same XRB subpopulation, namely BH XRBs in the high–soft state, dominates the cumulative emission at all time. On the contrary, the normalization of the SED does evolve with redshift. To zeroth order this evolution is driven by the cosmic SFR evolution. However, the metallicity evolution of the universe and the mean stellar population age are two important factors that affect the X-ray emission from HMXBs and LMXBs, respectively (see Figure 2).

The qualitative effects of an arbitrary X-ray radiation field in the formation and evolution of galaxies have already been studied. Hambrick et al. (2009) performed galaxy evolution simulations incorporating a UV and X-ray background field. They found that the gas properties at late times are significantly affected by the X-ray component resulting in a 30% increase of the warm gas component and a four-fold increase in the hot-dense gas component, while at the same time the formation of stars in small systems is reduced. Monte Carlo realizations of the merger and growth history of BHs show that X-rays from the earliest accreting BHs can provide such a feedback mechanism, on a global scale, finding that the first miniquasars globally warm the IGM and suppress the formation and growth of subsequent generations of BHs (Tanaka et al. 2012). More recently, Mesinger et al. (2013) ran semi-numerical simulations of the dark ages and the epoch of reionization, including both X-rays and UV radiation fields. They found that X-rays emitted from a XRB population can result in a more extended epoch of reionization and an overall more uniform reionization morphology, with the largest impact of X-rays being to govern the timing and duration of IGM heating.

All of the aforementioned studies consider either an arbitrary X-ray background field or one that is a mere extrapolation of observations from the local universe. In this letter we provide analytic prescriptions for the energy feedback from XRBs, based on our detailed synthetic models, which can be directly included in cosmological and galaxy formation and evolution simulations. These new prescriptions allow for the first time not only the qualitative but also the quantitative study of the effects of the energy feedback from XRBs in the early universe.

T.F. acknowledges support from the CfA and the ITC prize fellowship programs. S.N. is supported by NASA through an Einstein Postdoctoral Fellowship (contract PF2-130096).

REFERENCES

Aird, J., Nandra, K., Laird, E. S., et al. 2010, MNRAS, 401, 2531
Basu-Zych, A. R., Lehmer, B. D., Hornschemeier, A. E., et al. 2013a, ApJ, 762, 45
Basu-Zych, A. R., Lehmer, B. D., Hornschemeier, A. E., et al. 2013b, ApJ, 774, 152
Belczynski, K., Kalogera, V., & Bulik, T. 2002, ApJ, 572, 407
Belczynski, K., Kalogera, V., Rasio, F. A., et al. 2008, ApJS, 174, 223
Boroson, B., Kim, D.-W., & Fabbiano, G. 2011, ApJ, 729, 12
Boylan-Kolchin, M., Springel, V., White, S. D. M., Jenkins, A., & Lemson, G. 2009, MNRAS, 398, 1150
Croton, D. J., Springel, V., White, S. D. M., et al. 2006, MNRAS, 365, 11
Dib, S. 2011, ApJL, 737, L20
Dijkstra, M., Gilfanov, M., Loeb, A., & Sunyaev, R. 2012, MNRAS, 421, 213
Fabbiano, G. 2006, ARA&A, 44, 323
Faucher-Giguère, C.-A., Quataert, E., & Hopkins, P. F. 2013, MNRAS, 433, 1970
Fragos, T., Kalogera, V., Belczynski, K., et al. 2008, ApJ, 683, 346
Fragos, T., Kalogera, V., Willems, B., et al. 2009, ApJL, 702, L143
Fragos, T., Lehmer, B., Tremmel, M., et al. 2013, ApJ, 764, 41
Guo, Q., White, S., Boylan-Kolchin, M., et al. 2011, MNRAS, 413, 101
Haiman, Z. 2011, Natur, 472, 47
Hambrick, D. C., Ostriker, J. P., Naab, T., & Johansson, P. H. 2009, ApJ, 705, 1566
Hopkins, P. F., Quataert, E., & Murray, N. 2011, MNRAS, 417, 950
Hopkins, P. F., Richards, G. T., & Hernquist, L. 2007, ApJ, 654, 731
Justham, S., & Schawinski, K. 2012, MNRAS, 423, 1641
Lehmer, B. D., Alexander, D. M., Bauer, F. E., et al. 2010, ApJ, 724, 559
Lehmer, B. D., Xue, Y. Q., Brandt, W. N., et al. 2012, ApJ, 752, 46
Loeb, A., & Barkana, R. 2001, ARA&A, 39, 19
McClintock, J. E., & Remillard, R. A. 2006, in Compact Stellar X-Ray Sources, ed. W. Lewin & M. van der Klis (Cambridge Astrophysics Series, Vol. 39; Cambridge: Cambridge Univ. Press), 157
McQuinn, M., Hernquist, L., Zaldarriaga, M., & Dutta, S. 2007a, MNRAS, 381, 75
McQuinn, M., Lidz, A., Zahn, O., et al. 2007b, MNRAS, 377, 1043
Mesinger, A., Ferrara, A., & Spiegel, D. S. 2013, MNRAS, 431, 621
Mineo, S., Gilfanov, M., & Sunyaev, R. 2012a, MNRAS, 419, 2095
Mineo, S., Gilfanov, M., & Sunyaev, R. 2012b, arXiv:1207.2157
Mirabel, I. F., Dijkstra, M., Laurent, P., Loeb, A., & Pritchard, J. R. 2011, A&A, 528, A149
Ostriker, J. P., & Gnedin, N. Y. 1996, ApJL, 472, L63
Power, C., James, G. F., Combet, C., & Wynn, G. 2013, ApJ, 764, 76
Pritchard, J. R., & Furlanetto, S. R. 2007, MNRAS, 376, 1680
Sales, L. V., Navarro, J. F., Schaye, J., et al. 2010, MNRAS, 409, 1541
Silverman, J. D., Green, P. J., Barkhouse, W. A., et al. 2008, ApJ, 679, 118
Sobacchi, E., & Mesinger, A. 2013, MNRAS, 432, 3340
Sobolewska, M. A., & Życki, P. T. 2006, MNRAS, 370, 405
Springel, V., Di Matteo, T., & Hernquist, L. 2005, MNRAS, 361, 776
Stinson, G. S., Brook, C., Macciò, A. V., et al. 2013, MNRAS, 428, 129
Tanaka, T., Perna, R., & Haiman, Z. 2012, MNRAS, 425, 2974
Tremmel, M., Fragos, T., Lehmer, B. D., et al. 2013, ApJ, 766, 19
Tzanavaris, P., & Georgantopoulos, I. 2008, A&A, 480, 663
van Dokkum, P. G. 2008, ApJ, 674, 29
Wu, Y. X., Yu, W., Li, T. P., Maccarone, T. J., & Li, X. D. 2010, ApJ, 718, 620
Zhang, Z., Gilfanov, M., & Bogdán, Á. 2012, A&A, 546, 36